Available online at www.sciencedirect.com
SCIENCE DIRECT®
International Journal of Heat and Fluid Flow 25 (2004) 451–460
International Journal of HEAT AND FLUID FLOW
www.elsevier.com/locate/ijhff

Numerical and experimental study of separated flow in a plane asymmetric diffuser

Johan Gullman-Strand *, Olle Törnblom, Björn Lindgren, Gustav Amberg, Arne V. Johansson

Department of Mechanics, KTH, SE-100 44 Stockholm, Sweden

Abstract

Computations of the turbulent flow through plane asymmetric diffusers for opening angles from 8° to 10° have been carried out with the explicit algebraic Reynolds stress model (EARSM) of Wallin and Johansson [J. Fluid Mech. 403 (2000) 89]. It is based on a two-equation platform in the form of a low-Re $K-\omega$ formulation, see e.g. Wilcox [Turbulence Modeling for CFD, DCW Industries Inc., 1993]. The flow has also been studied experimentally for the 8.5° opening angle using PIV and LDV. The models under-predict the size and magnitude of the recirculation zone. This is, at least partially, attributed to an over-estimation of the wall normal turbulence component in a region close to the diffuser inlet and to the use of damping functions in the near-wall region. By analyzing the balance between the production and dissipation of the turbulence kinetic energy we find that the predicted dissipation is too large. Hence, we can identify a need for improvement of the modeling the transport equation for the turbulence length-scale related quantity.

Keywords: Plane asymmetric diffuser; Separated flow; Explicit algebraic Reynolds stress model; EARSM; Automated code generation

1. Introduction

Separation is common in many fluid flow applications. Separation can cause a substantial reduction of efficiency of a device, such as a diffuser. Hence, being able to predict separation accurately and in a time-efficient way is very desirable. The tested explicit algebraic Reynolds stress models (EARSM) increase the computational effort only slightly as compared to ordinary two-equation models, that rely on the eddy-viscosity hypothesis, while significantly more flow physics are captured. Therefore, EARSMs are strong candidates for becoming the next generation of industrial turbulence models. However, it is of great importance to also be aware of the limitations of this type of closure, an issue that will be addressed in this paper.

Flows in plane asymmetric diffusers (see Fig. 1) have previously been studied experimentally by Obi et al. (1993a,b), Buice and Eaton (1997) and Buice and Eaton (2000). However, in all these studies the angle of the inclined wall was 10° while we have chosen a slightly smaller angle of 8.5°. The reason for choosing a smaller opening angle in this project was to reduce the size of the separated region, and thereby, in combination with a high aspect ratio of the experimental diffuser, achieve a high degree of two-dimensionality of the mean flow. Furthermore, by investigating a plane asymmetric diffuser flow with an opening angle of 8.5°, which is almost on the verge of being fully attached (fully attached flow is predicted to occur for angles around 7°), the sensitivity to model details regarding separation prediction is increased.

Our intension, when using a two-dimensional test-case such as the plane asymmetric diffuser, is to have a case which: is challenging, demands a moderate computational effort, is simple to quantitatively compare with reference data and simplifies (as compared to a 3D-case) the task of drawing conclusions regarding the model behavior. Although one cannot generally expect a model that predicts a 2D separation correctly to do the same in a 3D-case, we chose a 2D-configuration since it still poses a great challenge to all existing turbulence models.

* Corresponding author. Tel.: +46-8-7907195; fax: +46-8-7969850.
E-mail address: johan@mech.kth.se (J. Gullman-Strand).

0142-727X/$ - see front matter © 2004 Elsevier Inc. All rights reserved.
doi:10.1016/j.ijheatfluidflow.2004.02.012

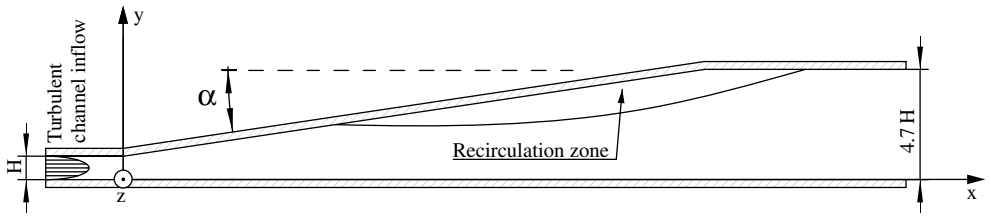

Fig. 1. The cross section of the diffuser. A part of the inlet channel is seen to the left and part of the outlet channel is seen to the right.

Simulations and model prediction studies on the geometry with 10° opening angle have been performed in a number of previous investigations. An extensive numerical study of the plane asymmetric diffuser flow was made by Kaltenbach et al. (1999), who performed a large eddy simulation (LES) at a Reynolds number, based on half inlet channel height and inlet channel friction velocity, of 1000. Their data showed good agreement with the experimental data by Buice and Eaton (2000) for mean velocity profiles. The location of the separation point also agreed well but some discrepancy was found in the location of the reattachment point. A possible reason for this can be the relatively small spanwise width ($4H$) of the computational domain which (when using periodic boundary conditions) tend to artificially enhance spanwise coherence of large scale structures. Kaltenbach et al. (1999) found that the subgrid-scale model plays an essential role in calculating the flow correctly, since sub-grid stresses contributed substantially (up to 8%) to the total shear stresses, at the resolutions used.

Other numerical studies using the Reynolds averaged Navier–Stokes (RANS) set of equations, involving more or less advanced closures based on eddy-viscosity models, (differential) Reynolds stress models and explicit algebraic Reynolds stress models, have been performed by a number of research groups. For instance, Apsley and Leschziner (2000) tested both linear and non-linear eddy-viscosity models as well as differential stress-transport models. They found that strain dependent coefficients and anisotropy resolving closures are needed. However, no models tested were capable of resolving all flow features in the diffuser. Apsley and Leschziner (2000) also point out the possibility to encounter problems related to 'flapping' motion of the unsteady separation. In an ERCOFTAC workshop (Hellsten and Rautaheimo, 1999), different numerical approaches with varying turbulence models were tested and compared to the Buice and Eaton (2000) data-set. Models used comprised $K-\varepsilon$, $K-\omega$, RSM and LES. The agreement was, for the more simple models, in general fairly poor indicating that more complex models are needed to capture the flow physics. The plane asymmetric diffuser has also been used as a test case for commercial codes. The investigation performed by Iaccarino (2000) aimed at finding the limits of the versatile commercial codes in this complex flow. The codes tested were CFX, Fluent and Star-CD. Two turbulence models were tested ($K-\varepsilon$ and $\overline{v^2}-f$) in these three codes. The results were compared to the Obi et al. (1993a) and Buice and Eaton (2000) data-sets. The $K-\varepsilon$ model was unable to capture the recirculation zone but the $\overline{v^2}-f$ model (Durbin, 1995) did so with an accuracy in separation length of 6%. The agreement for the friction coefficient was also fairly good.

In this study, two EARSMs are tested. The concept of an EARSM is to use an explicit relation between the individual Reynolds stress and the strain and rotation rates of the mean flow. The EARSM used in this study is described in Wallin and Johansson (2000) and the streamline curvature modeling is described in Wallin and Johansson (2002). The model will herein be referred to as WJ-EARSM.

In all figures in this article the coordinate system origin is located on the plane wall at the same streamwise position as the upstream corner of the inclined wall. The coordinate system is oriented according to Fig. 1. Mean velocities in the x, y and z directions are referred to as U, V and W respectively and velocity fluctuations are denoted by the corresponding lower-case letters. The Reynolds number based on the inlet channel height (H) and inlet channel bulk velocity (U_b) is 40 000 both in the experiment and in the computations.

2. The experiment

2.1. Description of the wind-tunnel

The experiments were performed in a closed loop wind-tunnel built specifically for this investigation. The wind-tunnel can be seen in Fig. 2. It consists of a blowing centrifugal fan delivering 11 kW of power followed by a section transforming the rectangular cross section shape of the blower outlet to another one with much higher aspect ratio. The transformer is followed by a straight duct (settling chamber) which contains two screens at its upstream end to even out mean flow variations. The settling chamber is followed by a two-dimensional contraction which is followed by a turbulence generating grid and a 3.2 m long inlet channel with a cross section area (width to height) of 1525×30 mm^2.

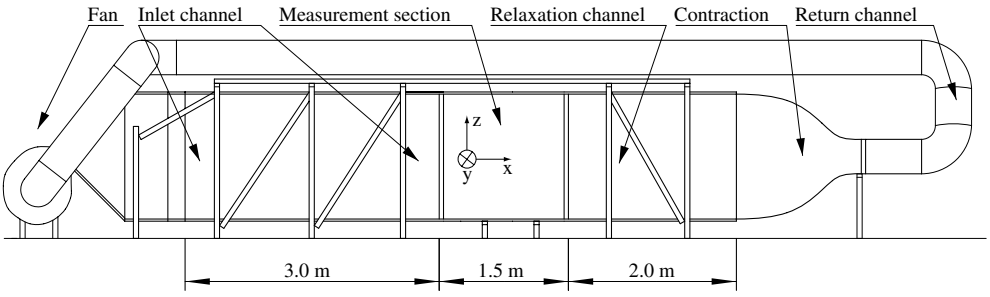

Fig. 2. The wind-tunnel used in the experiments. The flow is circulating counter clockwise.

The length to height ratio of the channel is thus larger than 100 ensuring fully developed channel flow at the downstream end (see e.g. Comte-Bellot, 1965). This is important in order to obtain a well-defined inlet condition to the diffuser which can be easily produced in numerical calculations. At the downstream end of the inlet channel, the end walls (limiting the spanwise width of the channel) are perforated with 2 mm holes. This section is 100 mm long and the end wall boundary layers are removed through these holes by means of suction to prevent end wall boundary layer separation in the diffuser. Such a separation would destroy the two-dimensionality of the mean flow.

The inlet channel is followed by the diffuser. The diffuser has an inclined wall on one side and a straight wall on the other. The inclined wall has an angle of 8.5°, see Fig. 1. At the upstream corner of the inclined wall there is a radius of approximately 100 mm to prevent separation at this corner. The straight wall and the end walls are made of Plexiglas to allow the use of optical measurement techniques such as LDV and PIV. The straight wall is equipped with pressure taps along the centerline in the downstream direction at an interval of 25 mm. There are also pressure taps in the spanwise direction 100 mm upstream the diffuser inlet on each side at 100 mm interval. These pressure taps are used to check the two-dimensionality of the incoming flow. The high aspect ratio, 50 at the diffuser inlet, is crucial to achieve a high degree of spanwise uniformity. The diffuser is followed by an outlet channel which is 141 mm high (4.7 inlet channel heights) and 2.5 m long. The purpose of this channel is to avoid upstream influence on the flow from devises located further downstream. This channel is partly made of Plexiglas to facilitate measurements. The outlet channel is followed by a transformation section, changing the aspect ratio of the cross section area towards unity. The contraction is followed by a heat exchanger which is necessary in a closed return wind-tunnel to keep the temperature steady. A temperature sensor is located in the outlet channel and a computer logged the temperature which was found to be steady within ±0.5 °C. A pipe with 400 mm diameter then leads the flow back to the fan. At the end of the pipe the seeding particles are injected into the flow. Just in front of the fan there is a slit ensuring constant pressure at the fan inlet.

2.2. Measurement techniques

The spanwise (z-direction) velocity component was measured using a one component LDV system. The measurement volume diameter using a lens with a focal length of 310 mm and a beam separation of 73 mm was 77 μm. The measurement volume length was 0.66 mm. The LDV was used in backscatter mode and was calibrated against a rotating wheel. The LDV measurements were made along the spanwise centerline of the diffuser at intervals of 50 mm. A total of 29 profiles were measured. In the wall normal direction, the interval varied with proximity to a wall and the downstream position, from 0.1 to 5 mm. Between 25 000 and 100 000 samples were taken at each measurement point and the time for collecting data was set to a minimum of 120 s per point.

In the streamwise and wall normal directions the velocity components were measured using PIV. A light-sheet, with a typical thickness of 1 mm, was produced using a 400 mJ double-pulse Nd-Yag laser and a digital double frame camera was used to image the illuminated particles. The CCD of the camera had 1018×1008 pixels and a gray-scale resolution of 8 bits. A $f = 60$ mm lens was used with a large ($f2.8$) aperture in order to get images over an area of about the size of the outlet channel height (141 mm) in both directions. 32×32 pixels (physical size 4.5×4.5 mm^2) interrogation areas with a 50% overlap were used. Sub-pixel interpolation assuming a Gaussian distribution was used in the cross-correlation analysis. The time between frames was optimized for each set of pictures and varied with the downstream position. To cover the entire measurement section PIV images were obtained at 11 downstream positions, 2048 image pairs were taken at each position. The image pairs (samples) were collected at a rate of 7.5 Hz and will thus be uncorrelated. Then, if one assumes the velocity distribution to be Gaussian, the statistical uncertainty for the second order moments with 2048 samples will, with 99% confidence, be less than 3%. It is known that a mean velocity gradient through the PIV

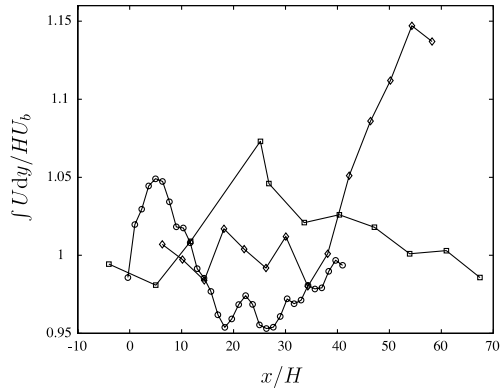

Fig. 3. Flow rate measured with PIV (◯) compared to measurements by Obi et al. (1993a) (◇) and Buice and Eaton (1997) (□).

interrogation areas can give rise to biased data. Therefore, it was always made sure, during the measurements, that the criterion for unbiased data suggested by Keane and Adrian (1992), $\Delta U\Delta t/d \leqslant 0.03$ was fulfilled, where ΔU is half the velocity difference over the interrogation area, Δt is the time between images and d is the physical interrogation area size. The LDV and PIV data were projected on a common grid with a mesh size of 10 mm × 2 mm in the streamwise and wall-normal directions respectively.

The flow rate is a good measure of the two-dimensionality of a flow and for this flow a suitable definition of the flow rate is

$$\frac{1}{HU_\mathrm{b}}\int U(y)\,\mathrm{d}y, \tag{1}$$

where U is the velocity in the x-direction, H is the inlet channel height and U_b is the bulk velocity of the inlet channel flow. Fig. 3 shows the flow rate measured with PIV in the center region of the measurement section. For comparison the flow rates of Obi et al. (1993a) and Buice and Eaton (1997) (the data have been taken from Kaltenbach et al., 1999) have been included in the figure.

3. Mathematical model

3.1. Base equations for the turbulence model

The Wilcox (1993) low-*Re* version of the transport equations for the turbulence kinetic energy, K, and inverse turbulence time-scale, ω, in the EARSM formulation are

$$\frac{\mathrm{D}K}{\mathrm{D}t} = \mathscr{P} - \beta^*\omega K + \frac{\partial}{\partial x_j}\left[(\nu + \sigma^*\nu_\mathrm{T})\frac{\partial}{\partial x_j}K\right], \tag{2}$$

$$\frac{\mathrm{D}\omega}{\mathrm{D}t} = \mathscr{P}_\omega - \beta\omega^2 + \frac{\partial}{\partial x_j}\left[(\nu + \sigma\nu_\mathrm{T})\frac{\partial}{\partial x_j}\omega\right], \tag{3}$$

$$\mathscr{P} = -\overline{u_i'u_j'}S_{ij} = -Ka_{ij}S_{ij}, \quad \mathscr{P}_\omega = \alpha\frac{\omega}{K}\mathscr{P} \tag{4}$$

with the low-*Re* functions

$$\alpha^* = \frac{\alpha_0^* + Re_\mathrm{T}/R_k}{1 + Re_\mathrm{T}/R_k}, \tag{5}$$

$$\alpha = \frac{5}{9}\,\frac{\alpha_0 + Re_\mathrm{T}/R_\omega}{1 + Re_\mathrm{T}/R_\omega}\,\frac{1}{\alpha^*}, \tag{6}$$

$$\beta^* = \frac{9}{100}\,\frac{5/18 + (Re_\mathrm{T}/R_\beta)^4}{1 + (Re_\mathrm{T}/R_\beta)^4}, \tag{7}$$

$$\begin{aligned} &\beta = 3/40,\\ &\sigma^* = \sigma = 1/2 \quad \alpha_0^* = \beta/3 \quad \alpha_0 = 1/10,\\ &R_k = 6 \quad R_\omega = 2.7 \quad R_\beta = 8,\\ &Re_\mathrm{T} = K/(\omega\nu). \end{aligned} \tag{8}$$

The near wall correction coefficients α, α^* and β^* are independent of wall normal distance, in contrast to the wall damping function f_1 of the EARSM, but instead contain the turbulence Reynolds number, or equivalently the ratio $K/\omega\nu$. The molecular viscosity is denoted ν. The near wall limiting behavior of K and ω are proportional to y^2 and y^{-2} respectively, hence $Re_\mathrm{T} \to 0$ as $y \to 0$.

3.2. Modification of the turbulence time-scale transport equation

Previously, one disadvantage of using the inverse of the turbulence time scale ω as complementary quantity to the kinetic energy, has been the difficulty to capture the singular behavior close to solid walls. The rapid variation is described by

$$\omega \to \frac{6\nu}{\beta y^2} \quad \text{for } y \leqslant 2.5\nu/u_\tau. \tag{9}$$

For the destruction and diffusion terms in Eq. (3), the singular behavior becomes especially troublesome since the terms behave as y^{-4} as $y \to 0$ in near-wall shear flow. A decomposition is introduced as $\omega = \tilde{\omega} + \omega_\mathrm{wall}$ with ω_wall given by Eq. (9) in the whole domain and $\tilde{\omega}|_{y=0} = 0$. The problem of computing the rapid growth of ω has now been transferred to handling the prescribed function ω_wall. The near wall diffusion and destruction terms associated with ω_wall cancel and Eq. (3) simplifies to

$$\begin{aligned}\frac{\mathrm{D}\tilde{\omega}}{\mathrm{D}t} = \mathscr{P}_\omega - \beta(\tilde{\omega}^2 + 2\tilde{\omega}\omega_\mathrm{wall}) + \frac{\partial}{\partial x_j}\left[(\nu + \sigma\nu_\mathrm{T})\frac{\partial}{\partial x_j}\tilde{\omega}\right]\\ + \frac{\partial}{\partial x_j}\left[\sigma\nu_\mathrm{T}\frac{\partial}{\partial x_j}\omega_\mathrm{wall}\right].\end{aligned} \tag{10}$$

In the EARSM context two terms on the right hand side are still singular at the wall ($\sim y^{-1}$). The main balance in

the immediate vicinity of the wall becomes $0 = -\alpha\omega_{\text{wall}}a_{ij}S_{ij} - 2\beta\tilde{\omega}\omega_{\text{wall}}$ from which we find that

$$\tilde{\omega}^+ \to -\frac{\alpha}{2\beta}a_{12} \quad \text{as } y^+ \to 0 \tag{11}$$

in a plane turbulent channel flow (note that $a_{12} \sim y^+$ as $y^+ \to 0$) and hence the singular near wall behavior has been eliminated when solving for $\tilde{\omega}$).

3.3. Explicit algebraic Reynolds stress model

We may consider differential Reynolds stress models (DRSM), (explicit) algebraic Reynolds stress models and eddy-viscosity based two-equation models as three different levels of the description of the evolution of the Reynolds stress anisotropy

$$a_{ij} = \frac{\overline{u_i'u_j'}}{K} - \frac{2}{3}\delta_{ij}. \tag{12}$$

In all three cases the turbulence kinetic energy and a length-scale determining quantity $(\varepsilon, \omega, \ldots)$, are determined from transport equations. For the DRSM case we may regard the six transport equations for $\overline{u_i'u_j'}$

$$\frac{\mathrm{D}\overline{u_i'u_j'}}{\mathrm{D}t} = \mathscr{P}_{ij} - \varepsilon_{ij} + \Pi_{ij} + \mathscr{D}_{ij} \tag{13}$$

as equivalent to a transport equation for K and a set of five transport equations for a_{ij}. Hence, the relative distribution of energy among the components is here governed by an equation where diffusive and advective effects are taken into account. In Eq. (13) the terms on the right-hand side describe production, dissipation, pressure–strain-related intercomponent transfer and diffusion, respectively.

At the EARSM level of anisotropy modeling, the advection and diffusion of a_{ij} are neglected in a chosen coordinate system. This is usually referred to as the weak equilibrium assumption (Rodi, 1976). Since the ε_{ij} and Π_{ij} tensors, in this context, are modeled as algebraic expressions in K, ε, a_{ij} and the mean velocity gradient tensor, the weak equilibrium assumption results in a local description of a_{ij} that can be expressed as

$$a_{ij} = a_{ij}(S_{ij}, \Omega_{ij}), \tag{14}$$

where

$$S_{ij} = \frac{\tau}{2}(U_{i,j} + U_{j,i}) \quad \text{and} \quad \Omega_{ij} = \frac{\tau}{2}(U_{i,j} - U_{j,i}) \tag{15}$$

are the mean strain and rotation tensors, normalized with the turbulence time-scale

$$\tau = \max\left(\frac{1}{\beta^*\omega}, C_\tau\sqrt{\frac{\nu}{\beta^* K\omega}}\right). \tag{16}$$

In Eq. (16), ν denotes the molecular viscosity, β^* from Eq. (7) is used and $C_\tau = 6.0$.

The EARSM rests on the same platform of two transport equations as eddy-viscosity based two-equation models. In such cases the anisotropy tensor is described by

$$a_{ij} = \text{const.} \times S_{ij}, \tag{17}$$

where the constant (in high-Re formulations) usually is referred to as $2C_\mu$.

Using the weak equilibrium assumption together with an isotropic assumption for the dissipation rate tensor and linear model for the pressure strain rate tensor one can derive an explicit algebraic equation for the anisotropy. The expression for the 2D case treated here reduces to evaluating the explicit relation

$$\mathbf{a} = f_1\beta_1\mathbf{S} + (1 - f_1^2)\frac{3B_2 - 4}{2\max(II_S, II_S^{\text{eq}})}\left(\mathbf{S}^2 - \frac{1}{3}II_S\mathbf{I}\right) + \left(f_1^2\beta_4 - (1 - f_1^2)\frac{B_2}{\max(II_S, II_S^{\text{eq}})}\right)(\mathbf{S}\Omega - \Omega\mathbf{S}) \tag{18}$$

with damping function

$$f_1 = 1 - \exp(-C_{y1}\sqrt{Re_y} - C_{y2}Re_y^2), \quad Re_y = \sqrt{K}y/\nu. \tag{19}$$

Coefficients $\beta_{1,4}$ and constants C_{y1}, C_{y2}, B_2 and II_S^{eq} from Wallin and Johansson (2000) are used. Boldface symbols represent matrix notation of the corresponding tensors, $\mathbf{I} = \delta_{ij}$ is the identity matrix and $II_S = S_{ik}S_{ki}$ is the second invariant of the mean strain-rate tensor. In Eq. (19), y is the wall normal distance.

Effects of system rotation and streamline curvature can also be captured in the EARSM through extensions analyzed by e.g. Girimaji (1997), Hellsten et al. (2002) and Wallin and Johansson (2002). This correction is based on a formal derivation of the weak equilibrium assumption in a streamline oriented curvilinear coordinate system. In the present paper this type of correction is not applied. It was tested and found to give small effects on the predictions for the present case.

3.4. Wall normal distance function

In turbulence modeling, the need to introduce the wall normal distance in i.e. damping functions often arises. This is also needed in the above defined ω_{wall} as well as the EARSM damping function f_1. In order to obtain the wall normal distance at any point in the domain, independent of the complexity of the boundary shape, a distance function is computed, using ideas from level set methods (Sethian, 1996). By solving the evolution equation

$$\frac{\partial\phi}{\partial t} - (1 - |\nabla\phi|) = \mu_\phi\nabla^2\phi \tag{20}$$

for the scalar ϕ in the whole domain with the solid wall boundary condition $\phi_{\text{wall}} = 0$, ϕ will take the value of the shortest wall normal distance for each node in the domain. A diffusion term with μ_ϕ acting as an artificial

viscosity, set proportional to the radius of the local element, is also introduced to damp noise and avoid swallow tail effects (Gullman-Strand (2002)). This enables the introduction of wall normal distance dependent equations, without the need to formulate mesh or domain specific functions. Equation (20) is solved before the flow calculations are initiated and the impact in computational time can thereby be considered to be minimal. The artificial viscosity μ_ϕ was successively reduced for the converged solution were the value in each node in the domain is equal to the wall normal distance. Hence $y = \phi$ in Eqs. (9) and (19). Paper in preparation by Gullman-Strand et al. (submitted for publication) that will explain and prove the concept further.

4. Numerical model

Introduction of automated code generation methodology in turbulence model development as well as practical engineering calculations drastically cuts down cycle time for the derivation of the numerical model and coding to a matter of minutes. It also presents the possibility to easily modify a generic set of governing equations for many types of flows.

Using the femLego toolbox (Amberg et al., 1999) together with an applied mathematics software (in this case Maple), the partial differential equations, the boundary conditions and initial conditions as well as the method of solving each equation are specified in a software worksheet and the FEM code is generated with the femLego toolbox from that sheet. The software presents the equations in a readable and adjustable format and all documentation is contained within the script. It also gives the possibility to derive the equations in the language of applied mathematics.

The fractional step method of Guermond and Quartapelle (1997), originally intended for the unsteady Navier–Stokes equations, was used for the RANS. The order of the finite elements can be chosen from within the worksheet, in this case piecewise linear elements (P1). Once the code is generated and compiled, the mesh is created by a generic unstructured mesh generator.

The unstructured mesh used in the present computations consisted in all three cases of 318×75 nodes in the streamwise and wall normal directions respectively, distributed in a structured fashion. The expanding part of the diffuser consisted of 100×75 nodes. Computations were also performed on a mesh at 8.5° with double node density (635×149) to confirm grid independence. A comparison of mean streamwise velocity between the coarse and fine mesh at 8.5° showed a difference in maximum reversed velocity of 3%. At $x/H = 20$ the relative error between the coarse and fine solution of the mean streamwise velocity and turbulence kinetic energy K is in the order of 0.4%. Figs. 4 and 5 show the two solutions and the negligible impact of grid refinement.

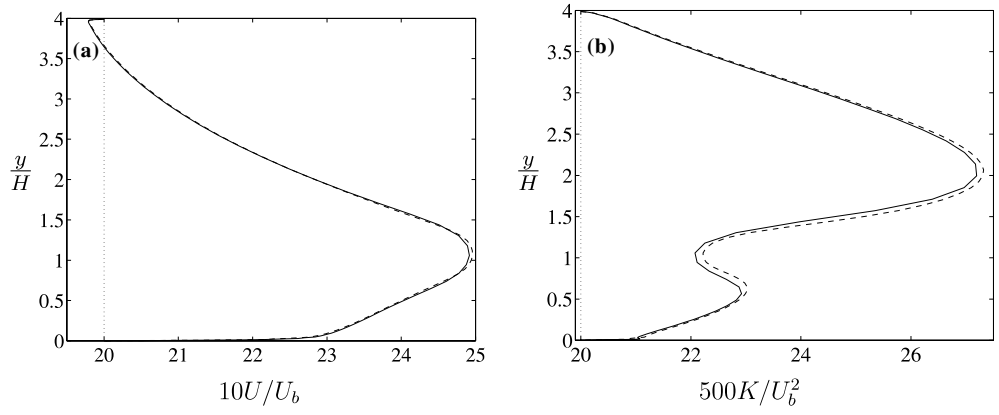

Fig. 4. (a) Mean streamwise velocity ($10\,U/U_\mathrm{b}$) and (b) turbulence kinetic energy ($500\,K/U_\mathrm{b}^2$) at $x/H = 20$ and 8.5°. Solid lines denote the coarse mesh and dashed line the fine mesh.

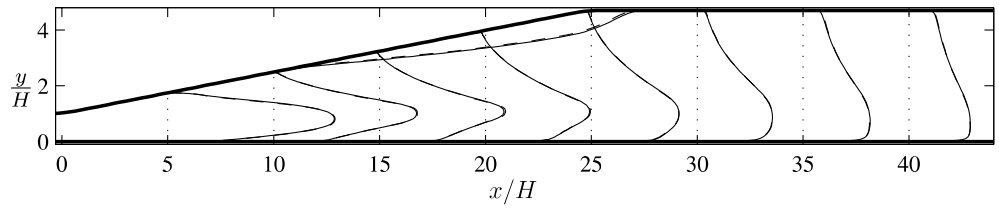

Fig. 5. Mean streamwise velocity ($10U/U_\mathrm{b}$) and dividing streamline. Legend as in Fig. 4.

The inlet conditions were obtained from channel flow calculations using the same computational code. The mesh was refined close to the wall with the first node placed at $0.35y_0^+$ in the inlet channel, increasing to $1.63y_0^+$ in the outlet channel, with y_0^+ denoting the wall unit distance in the inlet channel. This was sufficient to resolve the near wall behavior of the turbulence transport quantities in combination with the decomposition of the inverse turbulence time-scale ω.

5. Results

5.1. General description of the flow

When the fully developed turbulent channel flow enters the diffuser inlet it is subjected to a strong adverse pressure gradient. The turbulence here undergoes rapid changes. Thus, it is questionable if the assumption of negligible advection and diffusion of the Reynolds stress anisotropies, made in the EARSM, holds in this region. Other challenging phenomena arising in the region around the inlet are the streamline curvature effects when the flow turns around the convex upstream corner of the diffuser. For instance, the pressure coefficient curves in Fig. 8b reveal that a 'suction peak' is located on the convex wall giving first a favorable pressure gradient and then an adverse pressure gradient which is approximately twice as strong as the pressure gradient along the straight wall. Kaltenbach et al. (1999) found in their LES that a very small region of reversed flow was located at $x/H \approx 1.2$, this is not observed in the WJ-EARSM computation for this opening angle. However, the presence of this small region of reversed flow reported by Kaltenbach et al. (1999) has not yet been confirmed by any experiment.

Downstream of the diffuser inlet the mean flow stays attached to both the straight and the inclined wall until a large separation bubble forms on the inclined wall (see Fig. 6). Our PIV-data (for the 8.5° case) give a mean separation point at $x/H \approx 9$ and in the 10° case Buice and Eaton (1997) found it to be at $x/H \approx 8$. The back-flow coefficient χ (sometimes called reverse flow fraction), which has been measured in the present experiment, shows that instantaneous flow reversal occurs on the inclined wall from $x/H \approx 5$. The mean flow reattachment point was found in the exit channel at $x/H \approx 31$ in the present experiment and at $x/H \approx 26$ in the Buice and Eaton (1997) case.

5.2. Mean flow

We begin this comparison between model predictions and experimental results by studying the size and shape of the separation bubble. In Fig. 6, the dividing streamline, that separates the recirculating region from the outer mean flow, is depicted for the 8.0°, 8.5° and 10° cases. No experimental data are available for the 8.0° case (Fig. 6a), but the simulation indicates that the separation size diminishes rapidly for angles smaller than 8.5°. In order to investigate this further, simulations were performed for the case with 7.5° angle, and at that angle no region of backflow was obtained. In the 8.5° (Fig. 6b) case the mean separation point is almost the same in the computation as in the experiment, although this is difficult to see in the figure since the computed bubble is very thin near the separation point. The computed reattachment point is located at

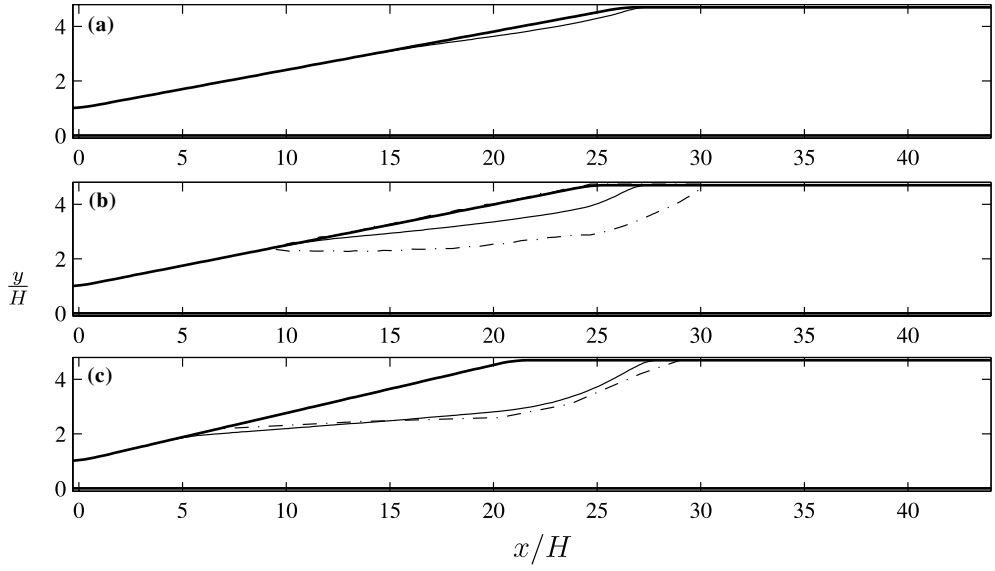

Fig. 6. Dividing streamline that separates the mean recirculation zone from the outer mean now for the cases (a) 8.0°, (b) 8.5° and (c) 10°. Solid lines show the standard WJ-EARSM and the experimental data is shown as dash-dotted lines.

$x/H \approx 27$ which is approximately four inlet channel heights upstream of the point measured in the experiments. Maybe more important than the prediction of the length of the bubble is the ability to predict its height, since this directly determines the character of the outer mean flow. The height of the computed separation bubble for the 8.5° case in Fig. 6b is approximately 60% of that in the experiment. For the 10° case comparisons are made with experimental data from Buice and Eaton (1997) and the agreement in height is good. The EARSM-predicted flow separates at $x/H = 4.5$ (also here the computed bubble is very thin in its most upstream part), which is $2.5H$ upstream of the separation point measured by Buice and Eaton (1997). The reattachment points agree well and they are located at $x/H = 28$ and 29 for the computation and the experiment, respectively.

Fig. 7 shows profiles of the mean velocity in the x-direction for the 8.5° and 10° cases. The qualitative shape of the computed profiles agrees rather well with the experimental data, especially in the 10° diffuser, but the strength of the backflow is under-predicted in both cases. The under-predicted size of the separation bubble in the computation of the 8.5° case has a large impact also on the outer flow field due to the smaller geometrical constriction that the bubble poses. The curvature correction of Wallin and Johansson (2002) has little significance in this geometry, at most in the order of 1% for all quantities when present.

Fig. 8a shows the skin friction coefficient, $C_f = 2\tau_w/(\rho U_b^2)$, along both the inclined and the straight diffuser wall for the 10° case. (Unfortunately, no skin friction data is currently available from the present experiment on the 8.5° diffuser.) The small region of separation found by Kaltenbach et al. (1999) on the convex surface at the diffuser inlet is not present in the EARSM solution. The difference in location of the separation point is easily seen here. The skin friction on the straight wall early in the diffuser is also decreasing faster in the computation than in the Buice and Eaton (1997) experiment. The computed velocity profiles in Fig. 7b are fuller than the experimental ones near the straight wall in the exit channel. This can also be seen in the C_f-curve as an over-predicted skin friction. As the

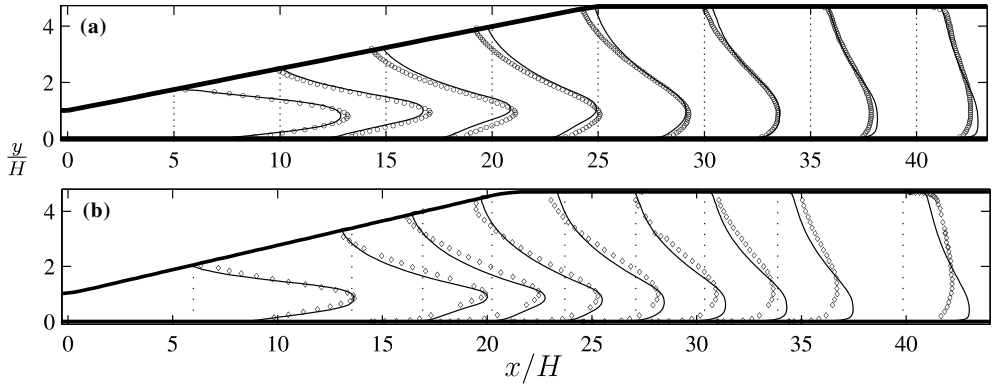

Fig. 7. U-velocity (parallel to the straight wall) for (a) the 8.5° case and (b) the 10° case, $10U/U_b$. Experiments (○) (data from Buice and Eaton, 1997 in (b)) and WJ-EARSM predictions (—). Dotted line shows zero-level at each position.

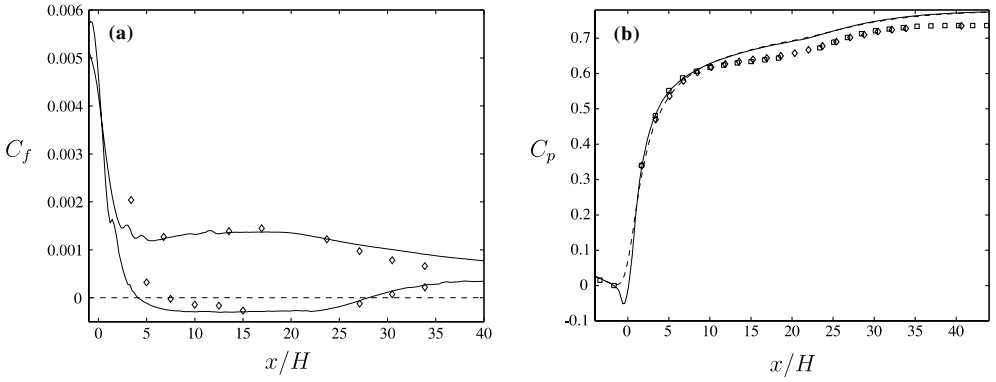

Fig. 8. (a) Skin friction and (b) pressure coefficients along the inclined and straight walls for the 10° diffuser. (a) WJ-EARSM (—), experimental data from Buice and Eaton (1997) (◇). (b) Computations inclined wall (—) and straight wall (- - -), experiments inclined wall (□) and straight wall (◇).

exit channel flow develops into a channel flow profile the skin friction coefficients will approach a value of approximately 3.5×10^{-4} at both walls.

5.3. Turbulence quantities

Since all three velocity components were measured in the current experiment it is possible to compare quantities such as the turbulence kinetic energy, $K=\overline{u_i'u_i'}/2$, or its production rate $\mathscr{P}=-\overline{u_i'u_k'}\partial U_i/\partial x_k$. The profiles of the kinetic energy shown in Fig. 9a show a rather good agreement in the most upstream part of the diffuser, but as we go downstream we see that the computed levels of K are smaller than the level measured in the experiment. The computed production rate in Fig. 9b exceeds the measured one in a major part of the diffuser, but is approximately at the measured level in the exit channel.

Hence, since the simulated production rate is larger than the experimental while the turbulence kinetic energy stays equal or is smaller in the simulation, the dissipation rate of turbulence kinetic energy must be over-predicted in the simulation.

In the upstream part of the diffuser the agreement between measurements and the computation is in general good. But the wall-normal component shown in Fig. 9c is larger in the computation and is an exception to this. The same behavior, although not as pronounced, can be observed in the simulation of the 10° case, see Fig. 10.

6. Discussion and concluding remarks

The use of near-wall damping functions in the low-*Re* formulation of the EARSM is not problem-free. The strength of the computed backflow is probably reduced by the damping function. The fact that the dissipation rate of turbulence kinetic energy was over-estimated in the computation indicates weaknesses in the modeling in the transport equation for the dissipation rate, or in this case the equation for ω. Especially the modeling of the production term and the turbulent diffusion term in this transport equation could be improved. A natural next step would be to test the diffusion model

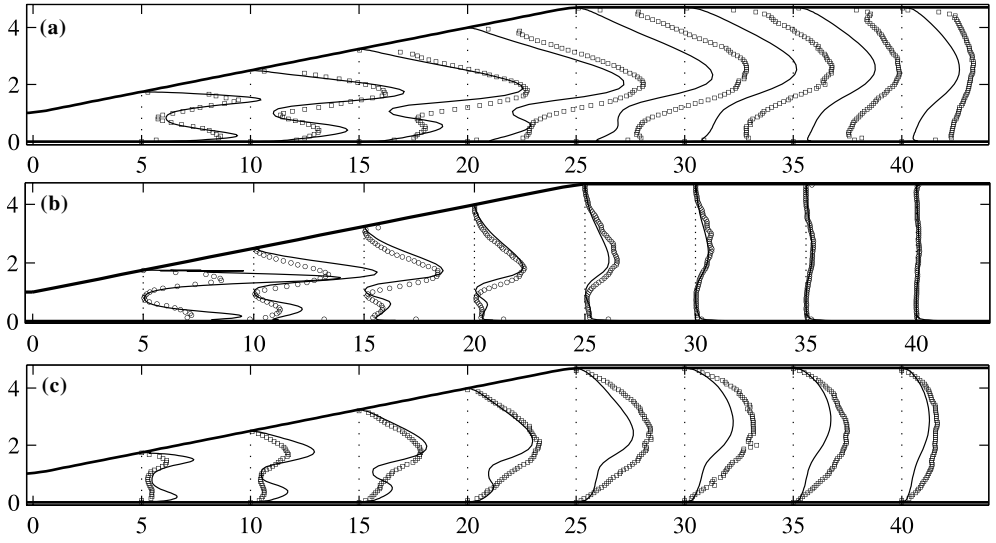

Fig. 9. Experimental data (◯) and WJ-EARSM (—) predictions for turbulence quantities for the 8.5° case: (a) turbulence kinetic energy ($500\ K/U_b^2$), (b) production rate of turbulence kinetic energy ($1500\ \mathscr{P}H/U_b^3$) and (c) variance of the wall-normal (y-direction) velocity component ($500\ \overline{v'^2}/U_b^2$). Dotted line shows zero-level at each position.

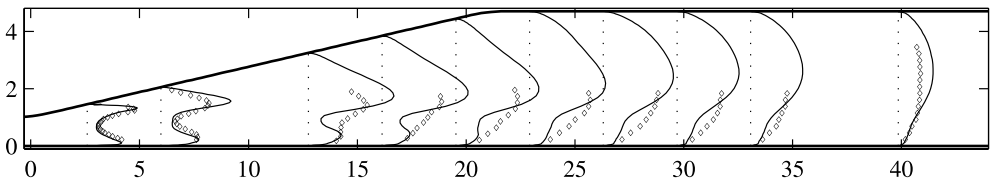

Fig. 10. Variance of the wall-normal velocity ($500\ \overline{v'^2}/U_b^2$) for the 10° case, experimental data by Buice and Eaton (1997) (◯) and WJ-EARSM (—). Dotted line shows zero-level at each position.

$$\frac{\partial}{\partial x_i}\left(c_\omega \frac{K}{\omega}\overline{u_i u_j}\frac{\partial \omega}{x_j}\right) \tag{21}$$

as suggested by Daly and Harlow (1970). Also recent progress by Hellsten (2004) with a recalibration of a zonal $K-\omega$ for external flow calculations contains possibilities for internal flows.

The over-prediction of the wall normal turbulence component is probably contributing to an exaggerated transport of mean flow momentum towards the inclined wall and hence to the delayed separation observed in the computation.

The 8.5° case has proven to be even more of a challenge to predict accurately using turbulence models than the 10° case. This can be attributed to the weaker adverse pressure gradient and to the flow being on the verge of being attached.

The methodology of generating a FEM-based CFD code through extensive use of automated code generation was demonstrated to be a feasible and attractive approach for analyzing the case of asymmetric diffuser flow for a set of different opening angles.

Acknowledgements

The authors like to thank the Swedish Energy Agency, the Swedish Strategic Research Council and the IVS Research School for financial support.

References

Amberg, G., Törnhardt, R., Winkler, C., 1999. Finite element simulations using symbolic computing. Mathematics and Computers in Simulation 44, 274–275.

Apsley, D.D., Leschziner, M.A., 2000. Advanced turbulence modelling of separated flow in a diffuser. Flow, Turbulence and Combustion 63 (1–4), 81–112.

Buice, C.U., Eaton, J.K., 1997. Experimental investigation of flow through an asymmetric plane diffuser. Technical Report. Department of Mechanical Engineering, Stanford University.

Buice, C.U., Eaton, J.K., 2000. Experimental investigation of flow through an asymmetric plane diffuser. Journal of Fluids Engineering 122, 433–435.

Comte-Bellot, G., 1965. Écoulement turbulent entre deux paroix parallèles. Publications scientifiques et techniques 419. Ministère de l'air, 2, Avenue de la Porte-d'Issy, Paris.

Daly, B.J., Harlow, F.H., 1970. Transport equations in turbulence. International Physics of Fluids 13, 2634–2649.

Durbin, P.A., 1995. Separated flow computations with the $k-\varepsilon-v^2$ model. AIAA Journal 33, 659–664.

Girimaji, S.S., 1997. A galilean invariant explicit algebraic Reynolds stress model for turbulent flows. Physics of Fluids 9, 1067–1077.

Guermond, J.L., Quartapelle, L., 1997. Calculation of incompressible viscous flow by an unconditionally stable projection fem. Journal of Computational Physics 132 (CP965587), 12–33.

Gullman-Strand, J., 2002. Turbulence modeling using automated code generation applied to asymmetric diffuser flow. Technical Report TRITA-MEK-02/06. Department of Mechanics, KTH, Sweden.

Gullman-Strand, J., Amberg, G., Johansson, A.V., submitted for publication. Mesh independent evaluation of wall distance for turbulent flow computations.

Hellsten, A., 2004. New advanced $k-\omega$ turbulence model for high-lift aerodynamics. In 42nd AIAA Aerospace Sciences Meeting and Exhibit. Reno, NV, USA, pp. 1–18.

Hellsten, A., Rautaheimo, P., (Eds.), 1999. Proceedings 8th ERCOFTAC/IAHR/COST Workshop on Refined Turbulence Modelling. Helsinki University of Technology.

Hellsten, A., Wallin, S., Laine, S., 2002. Scrutinizing curvature corrections for algebraic Reynolds stress models. In 32nd AIAA Fluid Dynamics Conference. St. Louis, MO, USA, pp. 1–15.

Iaccarino, G., 2000. Prediction of the turbulent flow in a diffuser with commersial CFD codes. Technical Report. Center for Turbulence Research.

Kaltenbach, H.J., Fatica, M., Mittal, R., Lund, T.S., Moin, P., 1999. Study of flow in a planar asymmetric diffuser using large-eddy simulation. Journal of Fluid Mechanics 390, 151–185.

Keane, R., Adrian, R., 1992. Theory of cross-correlation in PIV. Applied Scientific Research 49, 191–215.

Obi, S., Aoki, K., Masuda, S., 1993a. Experimental and computational study of separating flow in an asymmetric planar diffuser. In 9th Symposium on Turbulent Shear Flows, vol. 305. Kyoto, Japan, pp. 1–4.

Obi, S., Ohizumi, K., Aoki, K., Masuda, S., 1993b. Turbulent Separation Control in a Plane Asymmetric Diffuser by Periodic Perturbation. Elsevier Science. pp. 633–642.

Rodi, W., 1976. A new algebraic relation for calculating the Reynolds stresses. Zeitschrift für Angewandte Mathematik und Mechanik 56, 219–221.

Sethian, J.A., 1996. Level Set Methods and Fast Marching Methods. Cambridge University Press.

Wallin, S., Johansson, A.V., 2000. An explicit algebraic Reynolds stress model for incompressible and compressible turbulent flows. Journal of Fluid Mechanics 403, 89–132.

Wallin, S., Johansson, A.V., 2002. Modelling streamline curvature effects in explicit algebraic Reynolds stress turbulence models. Journal of Heat and Fluid Flow 23, 721–730.

Wilcox, D.C., 1993. Turbulence Modeling for CFD. DCW Industries Inc.